2D Monolayer of 1T’ Phase of Alloyed WSSe from Colloidal Synthesis

Ashkan Shahmanesh, Davide Romanin, Corentin Dabard, Sang-Soo Chee, Charlie Gréboval, Christophe Methivier, Mathieu G Silly, Julien Chaste, Matthieu Bugnet, Debora Pierucci, et al.

To cite this version:

Ashkan Shahmanesh, Davide Romanin, Corentin Dabard, Sang-Soo Chee, Charlie Gréboval, et al.. 2D Monolayer of 1T’ Phase of Alloyed WSSe from Colloidal Synthesis. Journal of Physical Chemistry C, 2021, 125 (20), pp.11058-11065. 10.1021/acs.jpcc.1c02275 . hal-03227064

HAL Id: hal-03227064
https://hal.science/hal-03227064v1

Submitted on 16 May 2021

2D Monolayer of 1T’ Phase of Alloyed WSSe from Colloidal Synthesis

Ashkan Shahmanesh[1], Davide Romanin[2], Corentin Dabard[2], Sang-Soo Chee[2], Charlie Gréboval[2], Christophe Methivier[3], Mathieu G. Silly[4], Julien Chaste[5], Matthieu Bugnet[6], Debora Pierucci[5], Abdelkarim Ouerghi[5], Matteo Calandra[2,7,8], Emmanuel Lhuillier[2*], Benoit Mahler[1*]

[1] Institut Lumière-Matière, CNRS UMR 5306, Université Lyon 1, Université de Lyon, 69622 Villeurbanne CEDEX, France.
[2]Sorbonne Université, CNRS, Institut des NanoSciences de Paris, 4 place Jussieu, 75005 Paris, France.
[3]Laboratoire de Réactivité de Surface, UMR CNRS 7197, Sorbonne Universités, 4 place Jussieu, F-75005 Paris, France.
[4] Synchrotron-SOLEIL, Saint-Aubin, BP48, F91192 Gif sur Yvette Cedex, France.
[5] Université Paris-Saclay, CNRS, Centre de Nanosciences et de Nanotechnologies, 91120, Palaiseau, Paris, France
[6] Université de Lyon, Université Claude Bernard Lyon 1, INSA Lyon, MATEIS, UMR CNRS 5510, 7 Avenue Jean Capelle, Villeurbanne Cedex 69621, France
[7] Department of Physics, University of Trento, Via Sommarive 14, 38123 Povo, Italy.
[8] Graphene Labs, Fondazione Istituto Italiano di Tecnologia, Via Morego, I-16163 Genova, Italy.

Abstract: We explore the colloidal growth of monolayers of WSSe alloy in their 1T’ phase with various Se content. We develop a synthetic procedure leading to reduced aggregation of the flakes. The presence of a narrow band-gap close to the top of the valence band has been evidenced combining photoemission spectroscopy and density functional theory (DFT). The electronic structure is weakly affected by the variation of the alloy content and atomic ordering. µ-Raman spectroscopy and STEM are used to confirm the obtained 1T’ phase, while simulations of the Raman spectra suggest contribution from both the S and Se atoms in the Raman spectra. Finally, we use electronic transport and photoconduction and reveal a short coherence length consistent with the defective nature of the flakes.

Keywords: Transition metal dichalcogenides, 2D monolayer, Density Functional Theory, Raman, Photoemission.

* To whom correspondence should be sent: el@insp.upmc.fr and benoit.mahler@univ-lyon1.fr

INTRODUCTION

TMDCs became a central building block for 2D nanophotonics[1,2] and optoelectronics.[3–5] Methods such as mechanical exfoliation and chemical vapor deposition have led to the highest quality samples. However, they are unsuitable to scale up for applications requiring a large amount of material as is the case for light-conversion[6], energy storage[7,8] or photocatalysis.[9] Therefore chemical growth appears as a more viable sample production path. Liquid phase exfoliations, in which small cations such as Li^+[10,11] coupled to solvent such as N-methyl-2-pyrrolidone (NMP),[12] have been proven as a viable strategy to obtain TMDC nanosheets.[13] However, the obtained materials are often aggregated and the control of the thickness at the single monolayer scale is still challenging.

Meanwhile, in the field of nanocrystals, great progresses have been achieved in the control of the nanoparticle shape in particular with synthesis of 2D nanoplatelets made of II-VI[14–16] and IV-VI[17] semiconductors. Surface chemistry can be controlled precisely and help toward the design of non-aggregated monolayer materials. In the vast list (MoS_2,[18] $MoTe_2$,[19] WS_2,[20] WSe_2[21]…) of TMDC materials[22] most of the efforts relative to colloidal synthesis have been focused on the growth of wide band gap semiconductors presenting a 2H phase,[23–27] which appears to be the most promising for optoelectronic applications.[13] On the other hand, the 1T' phase has been used as an efficient catalyst for hydrogen evolution[28] but less studies have been carried out on the growth of these 1T and 1T' phases[29–31] of TMDC materials using colloidal methods, and none of them have been dedicated to the growth of alloyed TMDC materials. Here, we investigate the growth of alloyed WSSe monolayers using a colloidal growth protocol. We propose a strategy that considerably favors the growth of TMDC monolayers in the 1T' phase only. Density Functional Theory (DFT) is then used to determine the band structure of the 1T' phase of $WSe_{2x}S_{2-2x}$ alloys and we found that, for all Se contents, the dispersion of the valence band is very stable with the introduction of defects. Beyond the stability of the electronic structure with the composition (*i.e.* alloy content), we also bring evidence that the gap in the vicinity of the Fermi level is not affected by local ordering of the S and Se atoms confirming that topological protection occurs in this material. To obtain more information on the structural properties of the system we also use Raman spectroscopy. Raman combined with TEM imaging confirms the 1T' nature of the grown flakes. The broadening of the Raman mode presents features of a low symmetry structure with contributions from both S and Se atoms, suggesting some kind of ordering of the S and Se atoms. Finally, we use electronic transport and photoconduction to further confirm the formation of the narrow band gap phase in 1T' $WSe_{2x}S_{2-2x}$ nanosheets.

METHODS

Materials: Octadecanthiol (ODT) (97%, TCI), oleylamine (OAm, 80%-90%, Acros), tungsten hexachloride (WCl_6, 99.9%, Sigma-Aldrich), carbon disulfide (CS_2, 99%, Sigma-Aldrich), trioctylphosphine (TOP, 97%, Aldrich), selenium powder (99.99%, Strem). All the materials were used as received with no additional purification.

Precursor: TOPSe (2.24 M): A 50 mL three-neck round-bottom flask was flushed with argon and maintained under an inert atmosphere. Trioctylphosphine (20 mL) was added, followed by 3.54 g selenium (44.83 mmol). The mixture was stirred for 72 hours until a colorless solution was obtained.

$WS_{2x}Se_{2-2x}$ synthesis: In a typical synthesis, 5 g octadecanethiol (32.4 mmol) was added to 15 mL oleylamine in a 50 mL three-neck flask and degassed under vacuum one hour at 80°C. After degassing, the mixture was heated up to 320 °C under argon atmosphere. 50 mg tungsten hexachloride (0.126 mmol) dissolved in 5 mL oleylamine was mixed with carbon disulfide (240 μL) and trioctylphosphine selenide (TOPSe 2.24 M, 560 μL). The injection mixture was added to the solvent into the flask dropwise (10 mL/h). At the end of the injection, the mixture was cooled down to room temperature and the product was centrifuged and washed 3 times with hexane and ethanol. The $WSe_{2x}S_{2-2x}$ nanosheets were dispersed in 10 mL toluene.

Annealing procedure: After filling a petri dish with ethylene glycol, 10 µL of the nanosheets solution is slowly dropped on top of it to prevent turmoil. After evaporation of the solvent (toluene), nanosheets would form a homogenous layer on top of the ethylene glycol. A glass slide is carefully stamped on top of the formed layer so that the thin layer would attach to it. After removing and drying with air blow, the glass slide is annealed on a hot plate at 380°C for 4 hours under controlled argon atmosphere.

TEM: TEM images were acquired on a JEOL JEM-2100 TEM equipped with a LaB6 electron source, operating at 200 kV. High resolution STEM images were obtained using a JEM-ARM200F Cold FEG NeoARM operating at 200 kV or 80 kV.

EDX analysis: The EDX spectra were recorded in a JEOL JEM-2100 TEM equipped with a LaB6 electron source. EDX analysis is used to determine the Se composition in the WSSe alloy.

PXRD: Diffractograms were acquired on a Malvern-Panalytical Empyrian diffractometer equipped with a copper Kα anode. Samples were prepared by aggregating the colloidal dispersion first using ethanol as a non-solvent and by drying the aggregates on a low-background silicon substrate.

µ-Raman spectroscopy: For Raman measurements, Si substrates were cleaned using bath sonication in acetone for 5 min, to remove organic agents and impurities. They were rinsed with isopropanol before N_2 blowing. Then, the sample solution was drop-casted onto a cleaned Si substrate and natively dried in air, to remove completely the solvent. Finally, the sample was rinsed in methanol for 30 sec to remove residue, and then dried by a nitrogen flow. Raman measurements were performed with a Labram-HR confocal microscope from Horiba, at room temperature and pressure using a 532 nm laser, with a power of 47 µW and a grating of 1800 g/mm. Low excitation power is required to prevent the sample heating which is observed to induce a phase transition toward the semiconducting 2H phase.

Electrode fabrication: We used optical lithography to make mono-digited electrodes with a length of 2.5 mm and a width of 20 µm. First, a Si substrate, with thermally grown 400 nm thick SiO_2 layer, was cleaned by bath sonication in acetone for 5 min. It was then rinsed by isopropanol before O_2 plasma treatment to remove organic residue. Adhesion promoter (Ti-prime) was spin-coated onto a cleaned substrate and baked at 120 ºC for 1 min. Then, AZ5214 photoresist was spin-coated and baked at 120 ºC for 2 min. After alignment, a substrate was exposed under UV lamp for 2 sec. Then, a second baking process was conducted at 120 ºC for 2 min to transform the type of resist, followed by a flood exposure for 40 sec. The resist was developed using AZ 726 for 30 sec and rinsed in deionized water for 30 sec. We then deposit 5 nm Cr/80 nm Au layer using a thermal evaporator. Finally, the lift-off was carried out by dipping the sample in acetone at room temperature for 30 min. The electrodes were then rinsed using isopropanol and dried by a nitrogen flow.

Transport measurements: The sample solution (10 mg mL^{-1}) was spin-coated onto the electrode at 1500 rpm for 1 min. Then, the sample was dipped in methanol for 30 sec to clean the residue, followed by a nitrogen flow. This step was repeated for 5 times to reach the desirable thickness (≈100 nm). The device was mounted on the cold finger of a closed cycle He cryostat. The chamber was brought under vacuum down to $\approx 10^{-3}$ mbar and connected to a Keithley 2634, which applies biases and measures the flowing current coming from samples. To characterize the samples under illumination, we used a 1550 nm laser.

RESULTS and DISCUSSION

In TMDC materials, the most striking physical properties (PL emission,[1] large on-off ratio field effect transistor[4]…) only arise for the most confined forms of the material (*ie* for the monolayers). Thus, when performing colloidal growth of such materials, it is critical to prevent aggregation and formation of multilayers. The latter can be controlled through the right choice of ligands.[21] In the previous reference, carboxylic acids have been used to prevent aggregation during growth, but it introduced at the same time oxide defects in the structure.[32,33] To avoid this issue, here we are instead using thiols as stabilizing ligands. In a large excess, they also complex the tungsten precursor to form thiolates. This bulky form of tungsten also slows down the reaction enabling a better control of the reactivity. In addition, it has been recently demonstrated that the addition of long ligands has a beneficial effect on the trap passivation, which leads to a photoluminescence enhancement in the case of the 2H phase.[32,33] This observation suggests that long ligands can be incorporated within the TMDC crystalline structure. For this synthesis, we use a combination of long chain amines and thiols (acting as solvent as well) and we slowly inject into the hot reaction mixture the tungsten and chalcogen precursors.

$$WCl_6 + CS_2 + TOPSe \xrightarrow[320°C]{\text{oleylamine, octadecanethiol}} WSSe_{ML} \tag{1}$$

Our synthetic scheme is depicted in equation (1). Tungsten chloride is first dissolved in oleylamine and is then mixed with carbon sulfide and trioctylphosphine selenide (respectively used as sulfur and selenium precursor). This mixture is then injected dropwise into a hot solution of oleylamine and octadecanethiol (from 280 to 320 °C depending on Se content). The mechanistic of the reaction follows the one WS_2 flakes growth previously described.[28] Briefly, CS_2 reacts with oleylamine, yielding oleylammonium oleylcarbamate. It thermally decomposes in oleylamine to give an excess of oleylammonium sulfide. This strong reducing agent can then reduce W(VI) to tungsten (IV) and Se (0) to Se (-II) that in turn react to produce WSSe monolayers.

At the end of the injection, the flakes are separated from the reaction medium by a series of precipitations. Finally, the nanosheets are dispersed and stored in a non-polar solvent such as toluene. The presence of octadecanethiol appears necessary to obtain well-dispersed monolayers. It prevents however the obtention of pure WSe_2 nanosheets. WSe_2 spectra presented in the following originate from multilayer nanostructures obtained using the same reaction scheme without octadecanethiol.

The final nanosheets dispersions are stable black solutions, exhibiting absorption spectra typical of the narrow-gap 1T' phase (**Figure 1**a). The spectra are almost featureless with an absorption increase at high energies. They remarkably do not present any feature in the 600-800 nm range where the exciton of the hexagonal wide band gap phase would have been expected, hinting the formation of phase-pure 1T' nanostructures. A first way to highlight the alloy formation is to phase change the metastable 1T' nanosheets into their semiconducting 2H counterpart. After annealing the flakes at high temperature (380 °C, see methods) under inert atmosphere, the absorbance spectra now are typical of the 2H phase (**Figure 1**b), with a clear excitonic transition appearing between 610 nm (pure WS_2) and 780 nm (pure WSe_2). As the Se content is increased, we observe a shift of this exciton to low energy, which confirms the introduction of the selenium into the TMDC lattice. This incorporation can also be observed from the X-ray diffraction patterns, see **Figure 1**c and its inset. A clear shift of the peak associated with the (110) planes is observed with the increase in the Se content and result from lattice parameter increase as Se is introduced in the WS_2 lattice.

The monolayers are small, disk-shaped, with a typical planar extension around 20 nm for all compositions (Figure S1). High-resolution scanning transmission electron microscopy (HRSTEM) imaging (**Figure 1**) Confirms the obtention of phase-pure 1T' $WS_{2-2x}Se_{2x}$ monolayers with the formation of "zig-zag" atomic tungsten lines, characteristic of the distorted 1T' structure (see atomic organization on **Figure 1**f and **Figure 3**b). It is easy to spot numerous tungsten atomic vacancies, or even bigger hole defects. These images, acquired at 200 kV do not allow to distinguish chalcogen atoms, as they do not have sufficient contrast compared to the background induced by the carbon support layer. Imaging at 80kV however (**Figure 1**e), induces sufficient interaction with the electron beam to allow to distinguish contrast variations induced by the composition variation in the chalcogen bilayer. Individual chalcogen atoms are still not distinguishable, but atomic couples are visible after 1T' to 2H phase transition induced by the electron beam (orange outlined area, **Figure 1**e and scheme **Figure 1**f). The extremely short-range contrast variations highlight the composition homogeneity of the alloyed monolayers.

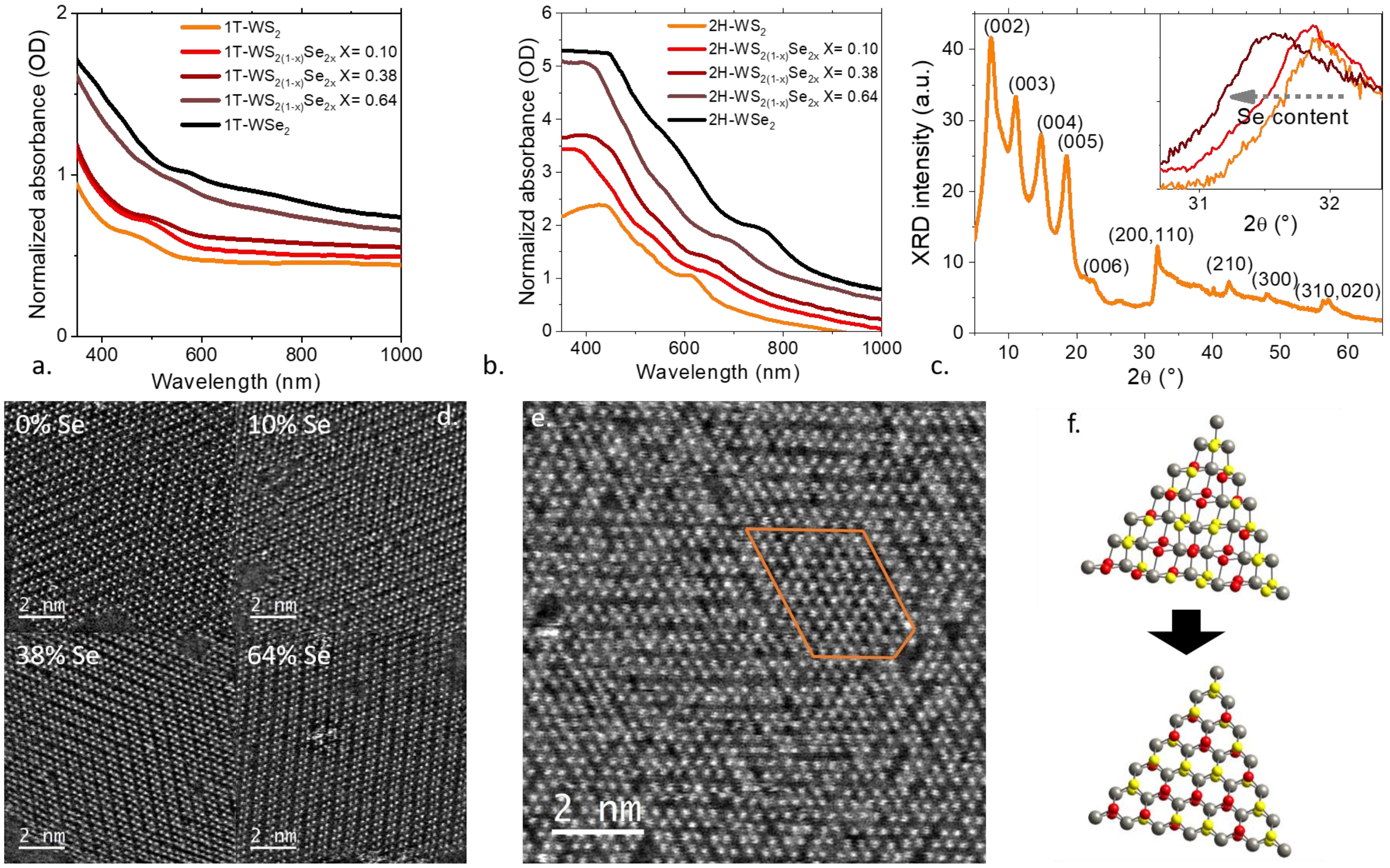

__Figure 1__. __Material synthesis and characterization__. (a.) Absorbance spectra of $WS_{2-2x}Se_{2x}$ dispersions with different Se content obtained after synthesis. (b.) spectra of the same samples obtained after thin film deposition and annealing at 370°C for 1h. (c.) X-ray diffractogram (Cu K_α as source - λ=0.154 nm) for monolayers of 1T' phase of WS_2. The inset shows the shift of the (110) peak while the Se content is increased. (d.) high angle annular dark field (HAADF) high-resolution scanning transmission electron microscopy (HRSTEM) images acquiered at 200kV of $WS_{2-2x}Se_{2x}$ monolayers obtained after synthesis exhibiting the 1T' phase for all the compositions. (e.) HRSTEM image obtained at 80kV of a $W(S_{0.36}Se_{0.64})_2$ 1T' monolayer in which the gray scale fluctuations corresponds to selenium/sulfur composition fluctuations, the orange-outlined area underwent a 1T'->2H phase transition, depicted in f.

Finally, energy dispersive X-ray spectroscopy can be used to quantify the Se content, see table 1. Selenium is observed in the final product even for a low introduced amount of selenium precursor. However, at high Se contents, the final S/Se ratio is lower than the one used for the precursors. This deviation is induced by a slow thermal decomposition of the thiols[34], which are then behaving as a sulfide source in this reaction making our synthetic approach not suited to obtain pure WSe_2 flakes.[8,29]

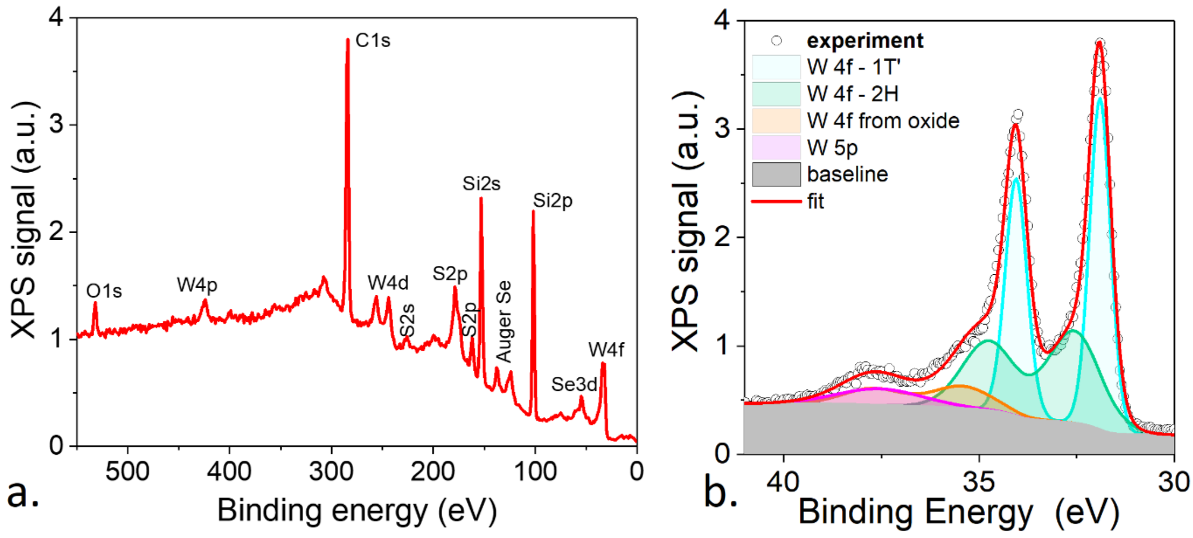

Figure 2. X-ray photoemission spectroscopy. *a. Photoemission overview spectrum of* $W(S_{0.62}Se_{0.38})_2$ *monolayer with 1T's phase film. b. Photoemission spectrum relative to the W4f state of* $W(S_{0.62}Se_{0.38})_2$ *monolayer flakes with 1T's phase. The two photoemission spectra are acquired at room temperature using a 1486.6eV photon energy.*

X-ray photoemission spectroscopy is then used to confirm this hypothesis, see **Figure 2**a-b and S2-3. To avoid charging effects during the measurements, we use an epitaxial graphene (graphene on SiC) substrate[35,36] allowing also to observe a clear valence band signal with no contributions from the substrate. The analysis of the W4f core level (**Figure 2**b) reveals four contributions. The main contribution with a binding energy (BE) of the $W4f_{7/2}$ state at 31.9 eV comes from a +IV oxidation state and is attributed to the 1T' phase. A second weaker contribution is present at BE($W4f_{7/2}$)=32.6 eV and is attributed to side growth of the hexagonal phase.[8,11,28] A third contribution appears at higher binding energies (BE($W4f_{7/2}$)=35.6 eV) corresponding to a +VI oxidation state resulting from oxides. The relative weight of this contribution is weak at low Se content, but is also clearly increased for the highest Se contents, see Figure S2. Finally, a last broad feature at BE(W5p)=36.9 eV is due to the W5p state. The analysis of the S2p and Se3d core levels are given in figure S3. Both of them require multi-components to be fitted, suggesting a complex environment. This picture is consistent with the presence of two sources of sulfur for WSSe: CS_2 and the thiols. The latter themselves are playing a double role of S source for the WSSe flake and of ligands[37] that stabilize the structure.

table 1 Alloy composition and electronic structure parameters for the WSSe flakes with various Se content

Volume TOPSe (mL)	**Se content (% atomic) from EDX**	**E_f-V_b (meV)**	**Work function (eV)**
0	0	53	4.16
0.17	10	55	4.27
0.56	38	100	4.29
1.68	62	190	4.22

Considering the states close to the Fermi level, we found the work function to be W_F=4.2±0.1 eV, almost constant with the Se content (figure S4 and table 1). The top of the valence band (V_b) is found to be very close to the Fermi level with E_f-V_b≈50-200 meV, see **Figure 3**d, S5 and table 1. The fact that the gap is preserved for all alloy composition confirms that the electronic structure is robust irrespective to the formation of alloys and possible presence of oxides.

To further unveil the material band structure, we use *ab initio* simulations based on DFT. The first step consists in determining the crystal structure of the WSSe flake. We considered two approaches to model two kinds of chalcogen distributions. First, a fully disordered structure is considered. In this case S and Se atoms are randomly occupying each chalcogen site. This configuration can be modeled by an effective atom (the virtual crystal approximation), whose wave function is made of the stoichiometric weight of each atom. In spite of being disordered, this configuration preserves all the symmetries existing in WS$_2$. The second approach relies on building periodic supercells and calculating the total energy for all the possible configurations in a supercell. Different supercell sizes and configurations compatible with stoichiometry have been tested, see figure S6-8a. The most stable structures are shown in Figure S6-8b and of course depend on the stoichiometry. However, as a general rule, S and Se atoms tend to organize along lines with S and Se atoms only, see **Figure 3**b-c. Only one of the lines is made of a mixture of the two atoms. We also include in our simulation the effect of the spin orbit coupling (SOC), which appears to be critical for the observation of a band gap (**Figure 3**b, S5 and S6-8d), [38] but seems to be irrelevant for the integrated valence band spectrum, see **Figure 3**d.

DFT simulations of the band structure are depicted in **Figure 3**a and S6-8 for the ordered and disordered configurations of WS$_{0.62}$Se$_{0.38}$. Once the SOC is considered, all phases present a narrow band gap (50-100 meV) in the vicinity of the Fermi level, which is consistent with previous experimental observations.[11] As a consequence, the projected density of states near the Fermi level matches fairly well the experimental data, see **Figure 3**d. We observe experimentally a broad feature which reflects the sparse density of states of the valence band. The electronic structure of WSSe in the 1T' phase determined by *ab initio* simulations appears very stable regardless of any form of disorder (presence of oxide, organization of S and Se atoms, alloying).

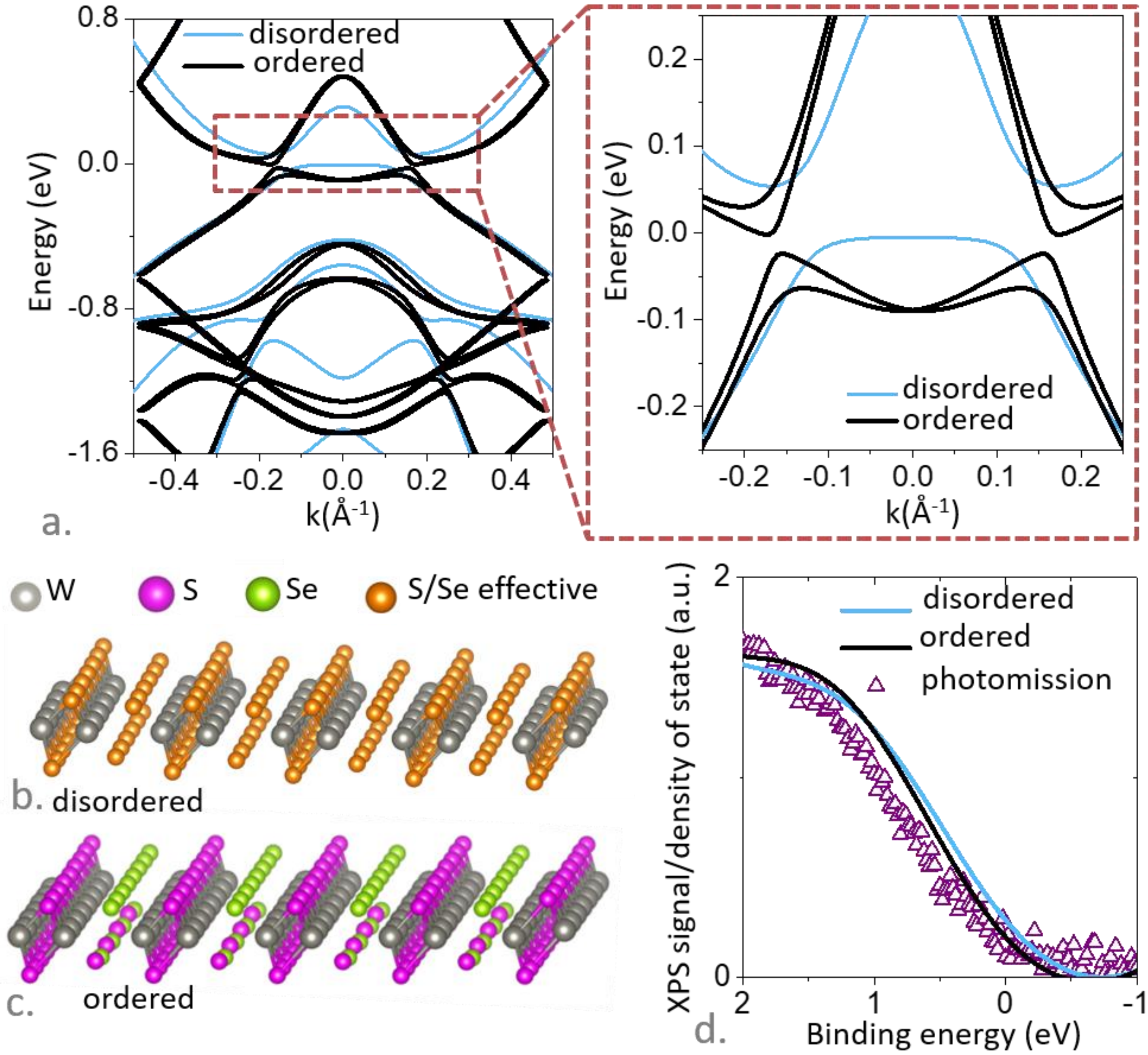

***Figure 3 Electronic spectrum of $WS_{0.62}Se_{0.38}$ monolayer flakes with 1T' phase**. a. Simulated band structure of the 1T' phase of $W(S_{0.62}Se_{0.38})_2$ for the most stable ordered structure and for a disordered structure in presence of spin-orbit coupling. The right part is a zoom around the Fermi level highlighting that the topological gap is preserved for both ordered and disordered structures. b. Ball-and-stick model of the disordered 1T' phase of $W(S_{0.62}Se_{0.38})_2$. In the case of the disordered structure effective S/Se atoms (orange spheres) are obtained by mixing the S and Se wavefunctions with the stoichiometric ratio. c. Ball-and-stick model of the most energetically favored configuration of the 1T' phase of $W(S_{0.62}Se_{0.38})_2$. Grey, magenta and green spheres correspond respectively to W, S and Se atoms. d. Valence band density of state for the disordered and for the most energetically favored configuration of the 1T' phase of $W(S_{0.62}Se_{0.38})_2$, compared with the valence band photoemission signal as a function of the binding energy.*

To study the structural properties of the flakes, we use Raman spectroscopy. The acquisition of spectra appears to be quite challenging since we observe a much weaker Raman signal than in the hexagonal phase. It was not possible to push the excitation power up as a clear transition from the 1T' distorted phase to the hexagonal phase is observed. The Raman spectra for three sample compositions are given in **Figure 4**a. Raman also confirms the presence of the 1T' phase with clear J_1 and J_2 peaks (120 cm^{-1}) that are not observed in the hexagonal structure.[39,40]

1T'-WS_2 shows clearly defined Raman peaks while the alloyed flakes only show broad features with an even much weaker intensity. In consequence, to better understand the Raman signal, the ab-initio Raman spectra have been computed via the LDA exchange-correlation functional (Figure S9). The fully disordered structure preserves all the symmetry of the WS_2 (top graph of **Figure 4**b and S10). Conversely, the ordered phase is less symmetric and thus a significant broadening of the Raman signal is expected (bottom graph of **Figure 4**b). In this sense, the experimental signal matches the one expected for the ordered structures better. Beyond the linewidth of the Raman mode, the A_{1g} mode also reinforces this hypothesis. In 1T'-WS_2, the A1g mode appears at ≈420 cm^{-1}. In the ordered structure, as Se is introduced within the lattice, this mode shifts toward lower energies following a $m^{-1/2}$ scaling, where m is the weighted mass of the effective S/Se atoms. Experimentally, this shift is not observed, and a mode keeps appearing at 420 cm^{-1} for all Se compositions, even if its intensity gets weaker. This picture is consistent with the fact that there is always a contribution for both types of atom, S and Se. The use of a virtual atom (disordered simulations in the virtual crystal approach) cannot capture this effect. This could suggest that some kind of ordering is present in the samples.

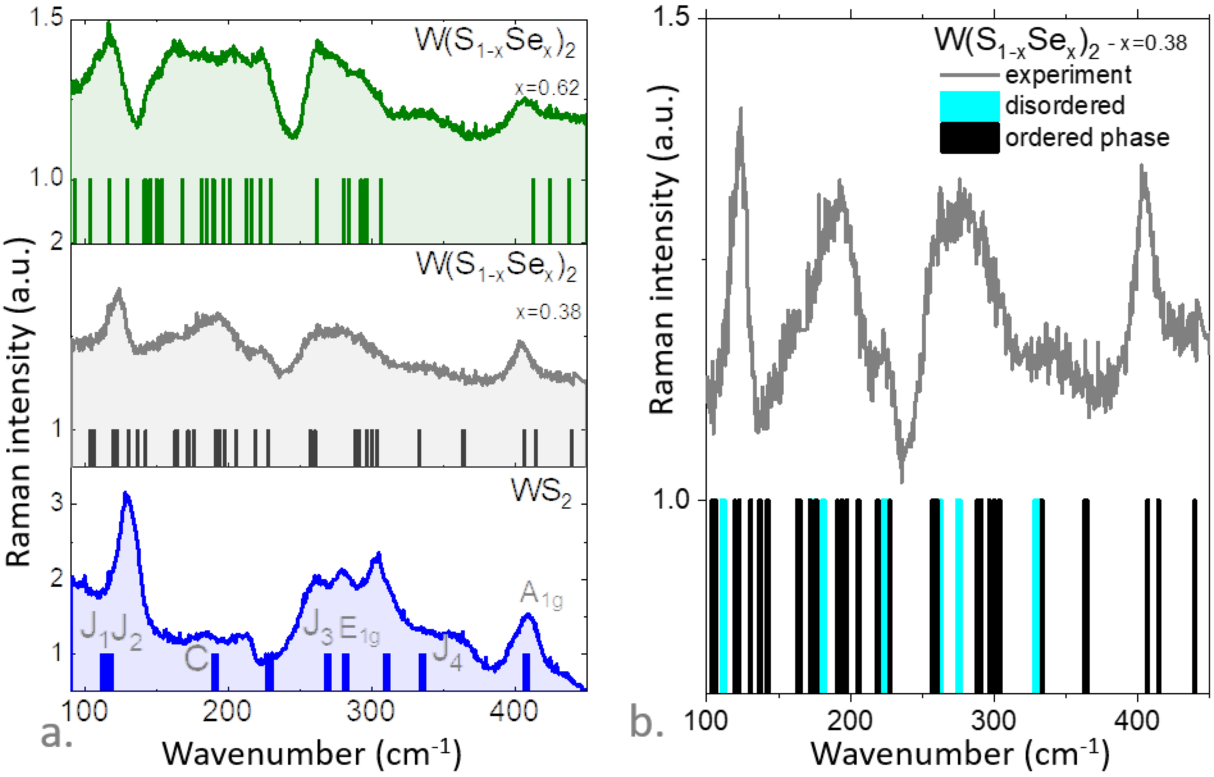

Figure 4 Vibrational properties. *a. Experimental (thick line) and simulated (histogram) Raman spectra for 1T' phase of WSSe for three Se contents. Simulations are provided for the ordered phases. b. Experimental (thick grey line) and simulated (red histogram for the ordered phase and green for the disordered phase) Raman spectra for 1T' phase of* $W(S_{0.62}Se_{0.38})_2$.

We finally probe the transport for an array of flakes deposited onto interdigitated electrodes, see a sketch of the device as inset of **Figure 5**a. Such array of particles appears to be conductive and presents a characteristic ohmic I-V. Under infrared illumination, at 1.55 µm (*i.e.,* far below the band gap of the hexagonal phase), we observe a photocurrent, see **Figure 5**b. This further confirms that the film is absorbing in the infrared, and is consequently made of a narrow band gap material. On the other hand, this response is slow (response time >>1 s) and in particular much longer that any radiative or non-radiative decay process (ns or ps). Due to its narrow band gap nature, WSSe flakes absorb the IR light. As carrier thermalize, they generate heat and increase the lattice temperature. The latter induces a change of the sample resistance and is the mechanism behind the observed photoresponse.

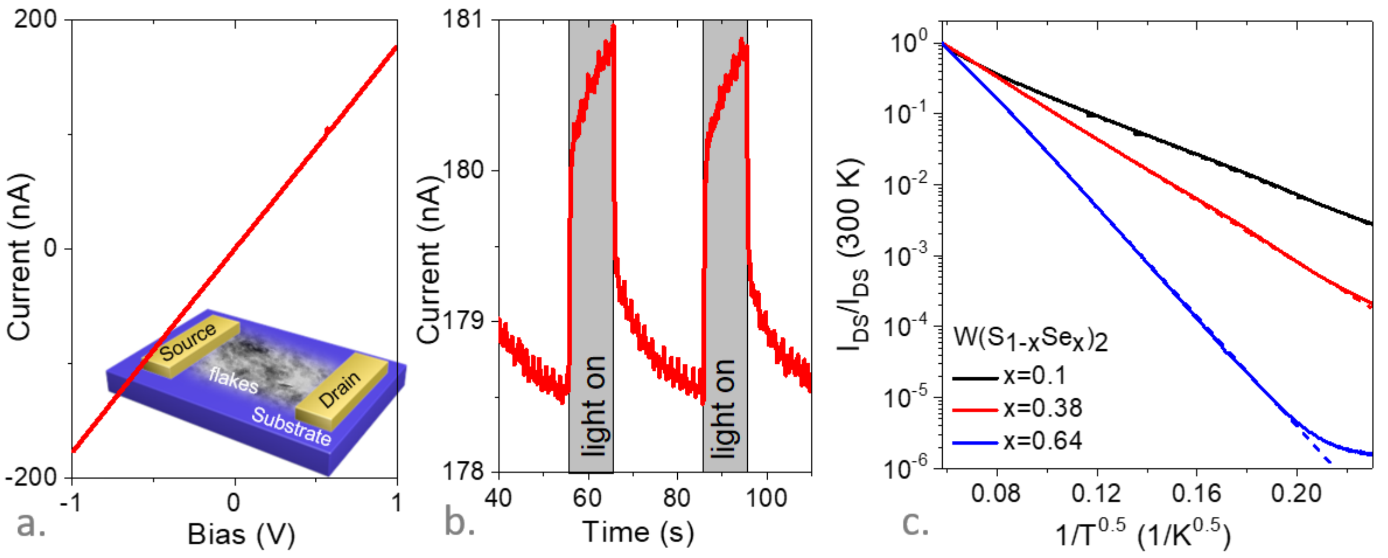

***Figure 5 Electronic transport from an array of $WS_{0.62}Se_{0.38}$ monolayer flakes with 1T' phase**. a. I-V curve at 50 K from an array of $W(S_{0.62}Se_{0.38})_2$ monolayer flakes with 1T' phase. The inset is a sketch of the device. b. Current as a function of time while the sample is illuminated by pulses of light at 1.55 µm (ie with a photon energy far below the absorption of the hexagonal phase of WSSe) for an array of $W(S_{0.62}Se_{0.38})_2$ monolayer flakes with 1T' phase. Measurement is carried out at 50 K. c. Current as a function of the temperature for WSSe monolayer flakes with 1T' phase with various Se content. The dashed lines are obtained using Efros-Shklovskii fit with the following expression-* $\sigma \propto \exp\left(-\left(T_{ES}/T\right)^{1/2}\right)$

As the sample is cooled, we observe a drop of the conductance, see **Figure 5**c. In such a disordered array of flakes, variable range hopping is expected to occur at low temperatures.[41] At short distance hopping occurs within the 2D flakes. At longer distance, interflake 3D hopping occurs since the film thickness (≈100 nm) is large with respect to the flake thickness (<1nm). In consequence, measurements of conductance according to the temperature have been carried out and have been fitted using Mott's law ($\sigma \propto \exp\left(-\left(T_M/T\right)^{1/4}\right)$, see Figure S11) and Efros-Shklovskii's law ($\sigma \propto \exp\left(-\left(T_{ES}/T\right)^{1/2}\right)$, see **Figure 5**c). The latter is found to fit more precisely the experimental data, what is typically the case for hopping between metallic grains[42] or strongly charged semiconductors.[43] The value of T_{ES} is found to be ≈2500 K for the sample with 38% Se content. From this temperature it is possible, in the 2D limit, to determine a transport correlation length through the expression $T_{ES} = \left(\frac{2.8e^2}{4\pi\varepsilon_r\varepsilon_0 k_B \zeta}\right)$ with e the proton charge, k_b the Boltzmann's constant, ε_0 the vacuum permittivity, ε_r the dielectric constant taken as the stoichiometry weighted value between WS_2 ($\varepsilon_r = 5.9$) and WSe_2 ($\varepsilon_r = 7.4$) values. We can estimate the coherence length to be 2.6 nm for this sample. This is typically smaller than the flake size observed by TEM, and consistent with their defective nature: presence of voids and vacancies.

Conclusions

We have developed a new synthetic colloidal growth method to obtain well-dispersed monolayers of $WSe_{2x}S_{2-2x}$ alloys in the 1T' phase. DFT simulations together with photoemission reveal a robust electronic structure nearby the Fermi level while the material is alloyed or gets oxidized, which can be interpreted as the signature of the topological protection at play in this system. µ-Raman spectroscopy is used to confirm that the material grows in its 1T'. LDA exchange-correlation potential simulation show a clear broadening of the Raman mode under alloying, which is only compatible with an ordered arrangement of the S and Se atoms. Finally, the electronic transport reveals a short coherence length consistent with the defective structure of the flake.

ACKNOWLEDGMENTS

The project is supported by ERC starting grant blackQD (grant n° 756225). We acknowledge the use of clean-room facilities from the “Centrale de Proximité Paris-Centre”. This work has been supported by the Region Ile-de-France in the framework of DIM Nano-K (grant dopQD). This work was supported by French state funds managed by the ANR within the Investissements d'Avenir programme under reference ANR-11-IDEX-0004-02, and more specifically within the framework of the Cluster of Excellence MATISSE and also by the grant IPER-Nano2 (ANR-18CE30-0023-01), Copin (ANR-19-CE24-0022), Frontal (ANR-19-CE09-0017), Graskop (ANR-19-CE09-0026) and NITQuantum. BM and MB acknowledge the use of the NeoARM instrument as part of the Consortium Lyon-St-Etienne de Microscopie. Computational resources for DFT simulations were provided by CINECA facilities, through the ‘ISCRA C’ project ‘HP10CY4S13’.

SUPPORTING INFORMATION

Supporting Information includes details about: 1. Material characterizations, 2. Electronic structure measurements, 3. DFT and vibrational simulation, 4. Electronic transport.

COMPETING INTEREST

The authors declare no competing financial interest.

REFERENCES

(1) Mak, K. F.; Lee, C.; Hone, J.; Shan, J.; Heinz, T. F. Atomically Thin MoS_2: A New Direct-Gap Semiconductor. *Phys. Rev. Lett.* **2010**, *105*, 136805.

(2) Wang, G.; Chernikov, A.; Glazov, M. M.; Heinz, T. F.; Marie, X.; Amand, T.; Urbaszek, B. Colloquium: Excitons in Atomically Thin Transition Metal Dichalcogenides. *Rev. Mod. Phys.* **2018**, *90*, 021001.

(3) Lopez-Sanchez, O.; Lembke, D.; Kayci, M.; Radenovic, A.; Kis, A. Ultrasensitive Photodetectors Based on Monolayer MoS_2. *Nat. Nanotechnol.* **2013**, *8*, 497–501.

(4) Radisavljevic, B.; Radenovic, A.; Brivio, J.; Giacometti, V.; Kis, A. Single-Layer MoS_2 Transistors. *Nat. Nanotechnol.* **2011**, *6*, 147–150.

(5) Noumbé, U. N.; Gréboval, C.; Livache, C.; Brule, T.; Doudin, B.; Ouerghi, A.; Lhuillier, E.; Dayen, J.-F. Ionic Glass–Gated 2D Material–Based Phototransistor: $MoSe_2$ over LaF_3 as Case Study. *Adv. Funct. Mater.* **2019**, *29*, 1902723.

(6) Lien, D.-H.; Amani, M.; Desai, S. B.; Ahn, G. H.; Han, K.; He, J.-H.; Ager, J. W.; Wu, M. C.; Javey, A. Large-Area and Bright Pulsed Electroluminescence in Monolayer Semiconductors. *Nat. Commun.* **2018**, *9*, 1229.

(7) Acerce, M.; Voiry, D.; Chhowalla, M. Metallic 1T Phase MoS_2 Nanosheets as Supercapacitor Electrode Materials. *Nat. Nanotechnol.* **2015**, *10*, 313–318.

(8) Zhou, P.; Collins, G.; Hens, Z.; Ryan, K. M.; Geaney, H.; Singh, S. Colloidal WSe_2 Nanocrystals as Anodes for Lithium-Ion Batteries. *Nanoscale* **2020**, *12*, 22307–22316.

(9) Voiry, D.; Salehi, M.; Silva, R.; Fujita, T.; Chen, M.; Asefa, T.; Shenoy, V. B.; Eda, G.; Chhowalla, M. Conducting MoS_2 Nanosheets as Catalysts for Hydrogen Evolution Reaction. *Nano Lett.* **2013**, *13*, 6222–6227.

(10) Voiry, D.; Yamaguchi, H.; Li, J.; Silva, R.; Alves, D. C. B.; Fujita, T.; Chen, M.; Asefa, T.; Shenoy, V. B.; Eda, G.; Chhowalla, M. Enhanced Catalytic Activity in Strained Chemically Exfoliated WS_2 Nanosheets for Hydrogen Evolution. *Nat. Mater.* **2013**, *12*, 850–855.

(11) Pierucci, D.; Zribi, J.; Livache, C.; Gréboval, C.; Silly, M. G.; Chaste, J.; Patriarche, G.; Montarnal, D.; Lhuillier, E.; Ouerghi, A.; Mahler, B. Evidence for a Narrow Band Gap Phase in 1T′ WS_2 Nanosheet. *Appl. Phys. Lett.* **2019**, *115*, 032102.

(12) Ng, H. K.; Abutaha, A.; Voiry, D.; Verzhbitskiy, I.; Cai, Y.; Zhang, G.; Liu, Y.; Wu, J.; Chhowalla, M.; Eda, G.; Hippalgaonkar, K. Effects Of Structural Phase Transition On Thermoelectric Performance in Lithium-Intercalated Molybdenum Disulfide ($LixMoS_2$). *ACS Appl. Mater. Interfaces* **2019**, *11*, 12184–12189.

(13) Eda, G.; Yamaguchi, H.; Voiry, D.; Fujita, T.; Chen, M.; Chhowalla, M. Photoluminescence from Chemically Exfoliated MoS_2. *Nano Lett.* **2011**, *11*, 5111–5116.

(14) Lhuillier, E.; Pedetti, S.; Ithurria, S.; Nadal, B.; Heuclin, H.; Dubertret, B. Two-Dimensional Colloidal Metal Chalcogenides Semiconductors: Synthesis, Spectroscopy, and Applications. *Acc. Chem. Res.* **2015**, *48*, 22–30.

(15) Diroll, B. T. Colloidal Quantum Wells for Optoelectronic Devices. *J. Mater. Chem. C* **2020**, *8*, 10628–10640.

(16) Nasilowski, M.; Mahler, B.; Lhuillier, E.; Ithurria, S.; Dubertret, B. Two-Dimensional Colloidal Nanocrystals. *Chem. Rev.* **2016**, *116*, 10934–10982.

(17) Schliehe, C.; Juarez, B. H.; Pelletier, M.; Jander, S.; Greshnykh, D.; Nagel, M.; Meyer, A.; Foerster, S.; Kornowski, A.; Klinke, C.; Weller, H. Ultrathin PbS Sheets by Two-Dimensional Oriented Attachment. *Science* **2010**, *329*, 550–553.

(18) Son, D.; Chae, S. I.; Kim, M.; Choi, M. K.; Yang, J.; Park, K.; Kale, V. S.; Koo, J. H.; Choi, C.; Lee, M.; Kim, J. H.; Hyeon, T.; Kim, D.-H. Colloidal Synthesis of Uniform-Sized Molybdenum Disulfide Nanosheets for Wafer-Scale Flexible Nonvolatile Memory. *Adv. Mater.* **2016**, *28*, 9326–9332.

(19) Sun, Y.; Wang, Y.; Sun, D.; Carvalho, B. R.; Read, C. G.; Lee, C.; Lin, Z.; Fujisawa, K.; Robinson, J. A.; Crespi, V. H.; Terrones, M.; Schaak, R. E. Low-Temperature Solution Synthesis of Few-Layer 1T ′-$MoTe_2$ Nanostructures Exhibiting Lattice Compression. *Angew. Chem.* **2016**, *128*, 2880–2884.

(20) Zhou, P.; Tanghe, I.; Schiettecatte, P.; van Thourhout, D.; Hens, Z.; Geiregat, P. Ultrafast Carrier Dynamics in Colloidal WS2 Nanosheets Obtained through a Hot Injection Synthesis. *J. Chem. Phys.* **2019**, *151*, 164701.

(21) Jung, W.; Lee, S.; Yoo, D.; Jeong, S.; Miró, P.; Kuc, A.; Heine, T.; Cheon, J. Colloidal Synthesis of Single-Layer MSe2 (M = Mo, W) Nanosheets via Anisotropic Solution-Phase Growth Approach. *J. Am. Chem. Soc.* **2015**, *137*, 7266–7269.

(22) Jeong, S.; Yoo, D.; Jang, J.; Kim, M.; Cheon, J. Well-Defined Colloidal 2-D Layered Transition-Metal Chalcogenide Nanocrystals via Generalized Synthetic Protocols. *J. Am. Chem. Soc.* **2012**, *134*, 18233–18236.

(23) Wang, S.; Zhao, J.; Yang, H.; Wu, C.; Hu, F.; Chang, H.; Li, G.; Ma, D.; Zou, D.; Huang, M. Bottom-up Synthesis of WS2 Nanosheets with Synchronous Surface Modification for Imaging Guided Tumor Regression. *Acta Biomater.* **2017**, *58*, 442–454.

(24) Barrera, D.; Wang, Q.; Lee, Y.-J.; Cheng, L.; Kim, M. J.; Kim, J.; Hsu, J. W. P. Solution Synthesis of Few-Layer 2H MX_2 (M = Mo, W; X = S, Se). *J. Mater. Chem. C* **2017**, *5*, 2859–2864.

(25) Giri, A.; Yang, H.; Thiyagarajan, K.; Jang, W.; Myoung, J. M.; Singh, R.; Soon, A.; Cho, K.; Jeong, U. One-Step Solution Phase Growth of Transition Metal Dichalcogenide Thin Films Directly on Solid Substrates. *Adv. Mater.* **2017**, *29*, 1700291.

(26) Sun, Y.; Fujisawa, K.; Lin, Z.; Lei, Y.; Mondschein, J. S.; Terrones, M.; Schaak, R. E. Low-Temperature Solution Synthesis of Transition Metal Dichalcogenide Alloys with Tunable Optical Properties. *J. Am. Chem. Soc.* **2017**, *139*, 11096–11105.

(27) Zhou, M.; Zhang, Z.; Huang, K.; Shi, Z.; Xie, R.; Yang, W. Colloidal Preparation and Electrocatalytic Hydrogen Production of MoS_2 and WS_2 Nanosheets with Controllable Lateral Sizes and Layer Numbers. *Nanoscale* **2016**, *8*, 15262–15272.

(28) Mahler, B.; Hoepfner, V.; Liao, K.; Ozin, G. A. Colloidal Synthesis of 1T-WS_2 and 2H-WS_2 Nanosheets: Applications for Photocatalytic Hydrogen Evolution. *J. Am. Chem. Soc.* **2014**, *136*, 14121–14127.

(29) Sokolikova, M. S.; Sherrell, P. C.; Palczynski, P.; Bemmer, V. L.; Mattevi, C. Direct Solution-Phase Synthesis of 1T' WSe_2 Nanosheets. *Nat. Commun.* **2019**, *10*, 712.

(30) Liu, Z.; Li, N.; Su, C.; Zhao, H.; Xu, L.; Yin, Z.; Li, J.; Du, Y. Colloidal Synthesis of 1T' Phase Dominated WS_2 towards Endurable Electrocatalysis. *Nano Energy* **2018**, *50*, 176–181.

(31) Sun, Y.; Fujisawa, K.; Terrones, M.; Schaak, R. E. Solution Synthesis of Few-Layer WTe2 and $Mo_xW_{1-x}Te_2$ Nanostructures. *J. Mater. Chem. C* **2017**, *5*, 11317–11323.

(32) Tanoh, A. O. A.; Alexander-Webber, J.; Xiao, J.; Delport, G.; Williams, C. A.; Bretscher, H.; Gauriot, N.; Allardice, J.; Pandya, R.; Fan, Y.; Li, Z.; Vignolini, S.; Stranks, S. D.; Hofmann, S.; Rao, A. Enhancing Photoluminescence and Mobilities in WS2 Monolayers with Oleic Acid Ligands. *Nano Lett.* **2019**, *19*, 6299–6307.

(33) Tanoh, A. O. A.; Xiao, J.; Alexander-Webber, J.; Pandya, R.; Li, Z.; Rao, A. Giant Photoluminescence Enhancement in $MoSe_2$ Monolayers Treated with Oleic Acid Ligands. *ArXiv200604505 Cond-Mat* **2020**.

(34) Yoo, D.; Kim, M.; Jeong, S.; Han, J.; Cheon, J. Chemical Synthetic Strategy for Single-Layer Transition-Metal Chalcogenides. *J. Am. Chem. Soc.* **2014**, *136*, 14670–14673.

(35) Pierucci, D.; Henck, H.; Naylor, C. H.; Sediri, H.; Lhuillier, E.; Balan, A.; Rault, J. E.; Dappe, Y. J.; Bertran, F.; Fèvre, P. L.; Johnson, A. T. C.; Ouerghi, A. Large Area Molybdenum Disulphide- Epitaxial Graphene Vertical Van Der Waals Heterostructures. *Sci. Rep.* **2016**, *6*, 26656.

(36) Henck, H.; Ben Aziza, Z.; Pierucci, D.; Laourine, F.; Reale, F.; Palczynski, P.; Chaste, J.; Silly, M. G.; Bertran, F.; Le Fèvre, P.; Lhuillier, E.; Wakamura, T.; Mattevi, C.; Rault, J. E.; Calandra, M.; Ouerghi, A. Electronic Band Structure of Two-Dimensional WS_2/Graphene van Der Waals Heterostructures. *Phys. Rev. B* **2018**, *97*, 155421.

(37) Voiry, D.; Goswami, A.; Kappera, R.; Silva, C. de C. C. e; Kaplan, D.; Fujita, T.; Chen, M.; Asefa, T.; Chhowalla, M. Covalent Functionalization of Monolayered Transition Metal Dichalcogenides by Phase Engineering. *Nat. Chem.* **2015**, *7*, 45–49.

(38) Choe, D.-H.; Sung, H.-J.; Chang, K. J. Understanding Topological Phase Transition in Monolayer Transition Metal Dichalcogenides. *Phys. Rev. B* **2016**, *93*, 125109.

(39) Jiménez Sandoval, S.; Yang, D.; Frindt, R. F.; Irwin, J. C. Raman Study and Lattice Dynamics of Single Molecular Layers of MoS_2. *Phys. Rev. B* **1991**, *44*, 3955–3962.

(40) Calandra, M. Chemically Exfoliated Single-Layer MoS_2: Stability, Lattice Dynamics, and Catalytic Adsorption from First Principles. *Phys. Rev. B* **2013**, *88*, 245428.

(41) Beloborodov, I. S.; Lopatin, A. V.; Vinokur, V. M.; Efetov, K. B. Granular Electronic Systems. *Rev. Mod. Phys.* **2007**, *79*, 469–518.

(42) Moreira, H.; Yu, Q.; Nadal, B.; Bresson, B.; Rosticher, M.; Lequeux, N.; Zimmers, A.; Aubin, H. Electron Cotunneling Transport in Gold Nanocrystal Arrays. *Phys. Rev. Lett.* **2011**, *107*, 176803.

(43) Martinez, B.; Livache, C.; Notemgnou Mouafo, L. D.; Goubet, N.; Keuleyan, S.; Cruguel, H.; Ithurria, S.; Aubin, H.; Ouerghi, A.; Doudin, B.; Lacaze, E.; Dubertret, B.; Silly, M. G.; Lobo, R. P. S. M.; Dayen, J.-F.; Lhuillier, E. HgSe Self-Doped Nanocrystals as a Platform to Investigate the Effects of Vanishing Confinement. *ACS Appl. Mater. Interfaces* **2017**, *9*, 36173–36180.

TOC graphic